catalysts

MDPI

Article

Nano-Hollow Zeolite-Encapsulated Highly Dispersed Ultra-Fine Fe Nanoparticles as Fischer–Tropsch Catalyst for Syngas-to-Olefins

Rui Hu, Tianye Wang, Yifan Wang, Yuan Zhu, Li Xie, Enhui Xing, Yu Wu and Zhijian Da *

Research Institute of Petroleum Processing, Sinopec, Beijing 100083, China
* Correspondence: dazhijian.ripp@sinopec.com

Abstract: A nano-hollow zeolite-encapsulating ultra-fine Fe nanoparticle catalyst denoted as Fe@$_{n\text{-}h}$S-HT was successfully synthesized through a simple water steam treatment of the Fe@$_{n\text{-}h}$S catalyst prepared by the "dissolution–recrystallization" (D-R) method. The Fe@$_{n\text{-}h}$S-HT catalyst had a hierarchical porous structure and a high dispersion of Fe_2O_3 particles with a size of 3.4 nm. Furthermore, the results of several characterization methods, such as XRD, HAADF-STEM, and H_2-TPR, further demonstrated the transformation of the skeleton Fe in Fe@$_{n\text{-}h}$S into Fe_2O_3, which was uniformly dispersed in the Fe@$_{n\text{-}h}$S-HT catalyst. Meanwhile, Fe@$_{n\text{-}h}$S-HT had significantly higher selectivity and yield of C_2-$C_4^=$ than the reference catalysts Fe/S and Fe@$_{n\text{-}h}$S, which provided strong proof for the confined catalysis of the metal@zeolite catalyst.

Keywords: hollow zeolite; Fischer–Tropsch synthesis; encapsulation; iron catalyst

Citation: Hu, R.; Wang, T.; Wang, Y.; Zhu, Y.; Xie, L.; Xing, E.; Wu, Y.; Da, Z. Nano-Hollow Zeolite-Encapsulated Highly Dispersed Ultra-Fine Fe Nanoparticles as Fischer–Tropsch Catalyst for Syngas-to-Olefins. *Catalysts* **2023**, *13*, 948. https://doi.org/10.3390/catal13060948

Academic Editor: Izabela Czekaj

Received: 28 April 2023
Revised: 21 May 2023
Accepted: 22 May 2023
Published: 30 May 2023

1. Introduction

Owing to the high reaction activity of nanoparticles, the research and application of (sub)nanometric metal catalysts derived from nanoscience and nanotechnology have attracted great attention in recent years [1,2]. Nevertheless, it cannot be ignored that the high surface energy due to the decrease in particle size will lead to poor thermodynamic stability of the active phase in the catalyst. Especially when the metal particles are loaded on the surface of conventional supports, they are more likely to migrate, aggregate, or even sinter under high temperatures, resulting in catalyst deactivation, which limits their practical application in the field of heterogeneous catalysis [3,4]. To address this issue, confining the metal nanoparticles in the inner channels of porous supports such as γ-Al_2O_3, zeolite, MOFs, porous carbon, and mesoporous silica, among others, helps to resist the aggregation, resulting in the high stability of the catalysts [1,4]. Among these porous supports, zeolites have been proven to be ideal candidates for embedding metal nanoparticles due to their uniform micropores, unique shape selectivity, and high hydrothermal stability, which have been widely applied in the catalytic process.

In recent years, metal@zeolite catalysts have attracted much interest due to their superior catalytic performance enhancement in many fields. Niu et al. [5] reported a maximum aviation fuel selectivity of 45% over the hollow hierarchical Silicalite-1 zeolite-encapsulated PtNi bi-metal nanoparticle catalyst PtNi@S-1, employed for the hydroconversion of methyl stearate into aviation fuel range alkanes. The results showed that both the selectivity of the products and the stability of PtNi@S-1 were significantly higher than those of the PtNi/S-1 catalyst synthesized via the conventional impregnation method. Ma et al. [6] researched the catalytic performance in the dry reforming of methane with high loading and uniform Ni nanoparticles encapsulated in Silicalite-1 zeolite, of which the sizes of Ni NPs were maintained at ca. 4–5 nm and the TOF kept at 60 s^{-1} (800 °C) by increasing the Ni loading from 3% to 20%. The evaluation results showed that the catalysts with various Ni loadings all exhibited high stability upon running for 150 h. Furthermore,

Kang et al. [6] reported a Silicalite-1 zeolite-encapsulating sodium-modified rhodium nanoparticle catalyst (Na-Rh@S-1). They revealed that the Na-Rh@S-1 catalyst exhibited a higher dispersion of Rh nanoparticles and more outstanding activity for the CO_2 hydrogenation to ethanol reaction.

Although metal@zeolite catalysts have attracted much attention and have shown excellent catalytic performance in several fields, the research into Fe nanoparticles embedded in zeolite is relatively less than that into other metals such as Ni, Cu, Co, and noble metals. The reason for this is that the Fe species is easy to substitute in the zeolite framework [7,8] with the assistance of organic ligands and templates. In addition, Fe-based catalysts have been researched and used the most for Fischer–Tropsch (F-T) synthesis owing to their high availability, favorable light olefin selectivity, and elevated water–gas shift (WGS) reaction activity [9–11]. For instance, Fang et al. [12] reported a core–shell structure catalyst, FeMn@C, which was employed for the Fischer–Tropsch synthesis reaction. This catalyst exhitibited excellent activity, high light olefin selectivity (40.6%), and stability. Therefore, in this work, to adequately integrate the uniqueness of the Fe-based catalyst for the F-T reaction and the confinement effect of metal@zeolite catalysts, the Fe species encapsulated in nano-hollow S-1 zeolite were prepared via the D-R method, which was denoted as Fe@$_{n\text{-}h}$S. Meanwhile, to address the issue that Fe species are easy to substitute in the zeolite framework, resulting in the poor activity of Fe-based catalysts in the F-T reaction, a mild water steam aging treatment was conducted for the Fe@$_{n\text{-}h}$S catalyst. Through this novel and easy method, the highly dispersed ultra-fine α-Fe_2O_3 nanopaticle encapsulated in the S-1 zeolite catalyst, denoted as Fe@$_{n\text{-}h}$S-HT, was successfully synthesized. Furthermore, the results of several characterization methods, such as XRD, HAADF-STEM, and H_2-TPR, further demonstrated the transformation of skeleton Fe in Fe@$_{n\text{-}h}$S into Fe_2O_3, which was uniformly dispersed in the Fe@$_{n\text{-}h}$S-HT catalyst. Not only that, but the evaluation results of the F-T reaction also showed that the Fe@$_{n\text{-}h}$S-HT catalyst had significantly higher selectivity and yield of C_2-$C_4^=$ than the reference catalysts Fe/S and Fe@$_{n\text{-}h}$S, which provided strong proof for the confined catalysis of the metal@zeolite catalyst.

2. Results and Discussion

2.1. Textural Characteristics and N_2 Physisorption

The textural properties of the parent S-1 zeolite and the catalysts were characterized by N_2-BET and are depicted in Figure 1. As shown in Figure 1A, the parent S-1 and Fe/S show the same type of isotherms, which indicates that the loading of active metals has little effect on the structure of the silicalite-1 zeolite. For Fe@$_{n\text{-}h}$S and Fe@$_{n\text{-}h}$S-HT, the displayed type-IV isotherms with H2 hysteresis loop, which consist of an abrupt step at around p/p_0 = 0.45, are characteristic of the phenomenon of the pore-blocking effect [13,14]. This feature implies that there was an ink-bottle pore system in the samples, which means that the zeolite has cavities connected to the outside through narrow channels (<4 nm) [5,15]. Additionally, for all the samples, the steep increase in adsorption quantity and the hysteresis curve at high relative pressure (p/p_0 > 0.9) demonstrate the existence of mesopores derived from the aggregation of zeolite crystals [5]. The NLDFT pore size distribution curves presented in Figure 1B further confirm that the Fe@$_{n\text{-}h}$S and Fe@$_{n\text{-}h}$S-HT catalysts possess a hierarchical porous structure, and the size of the mesopores generated from the TPAOH treatment is concentrated at 3~4 nm. However, the parent S-1 and Fe/S samples mainly present microporous structures, and a small quantity of mesoporous structures can be observed at 2~4 nm, which are inter-crystalline mesopores generated by the aggregation of zeolite crystals.

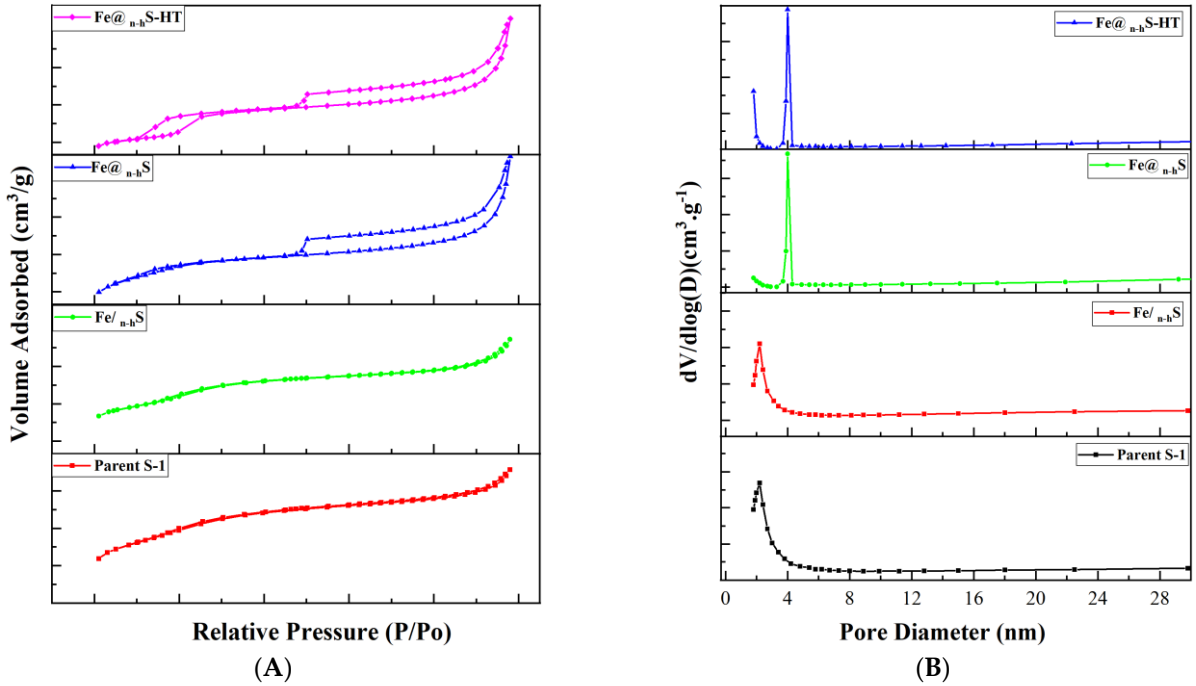

Figure 1. (**A**): N_2 absorption–desorption isotherm curves; and (**B**): pore size distributions of all the samples.

The textural properties of all the samples derived from the N_2-BET experiment are summarized in Table 1. It can be observed that the parent S-1 possessed the largest specific surface area (407.07 $m^2 \cdot g^{-1}$) and microporous specific surface area (367.68 $m^2 \cdot g^{-1}$). After impregnation, the specific surface and the total volume of Fe/S decreased slightly since the metal was deposited on the micropores and external surfaces of the catalysts. In addition, the specific surface of Fe@$_{n\text{-}h}$S decreased by 1.02% compared to the Fe/S sample due to its smoother crystal surface caused by the recrystallization process [5,16]. Compared to Fe/S, Fe@$_{n\text{-}h}$S exhibited both a smaller microporous specific area decrease (2.75%) and a larger external specific area increase (14.61%), which suggests the formation of mesopores during the encapsulation process [5]. In addition, compared to Fe/S and Fe@$_{n\text{-}h}$S, the specific area of Fe@$_{n\text{-}h}$S-HT decreased by 13.49% and 12.60%, respectively. However, the microporous specific area of Fe@$_{n\text{-}h}$S-HT increased significantly compared to Fe/S and Fe@$_{n\text{-}h}$S, which was contrary to the change in the S_{BET}. It was speculated that the Fe originally grown on the skeleton of the zeolite transformed into FeO_x particles during the water steam treatment process and entered the zeolite cavity formed during the dissolution recrystallization process. Furthermore, the mesoporous pore volume of Fe@$_{n\text{-}h}$S and Fe@$_{n\text{-}h}$S-HT calculated by "V_{total}-V_{micro}" significantly increased compared to Fe/S. These results further confirm that Fe@$_{n\text{-}h}$S and Fe@$_{n\text{-}h}$S-HT possess a hierarchical porous structure, which is in agreement with the experimental results reported for hollow MFI zeolites [17,18].

Table 1. Textual Properties of Parent S-1 Zeolite and Series Catalysts.

Samples	S_{BET} [a] (m^2/g)	S_{micro} [b] (m^2/g)	$S_{meso/ext}$ [c] (m^2/g)	V_{total} [d] (cm^3/g)	V_{micro} [b] (cm^3/g)
Parent S-1	407.07	367.68	39.39	0.2441	0.1754
Fe/S	386.21	347.82	38.39	0.2392	0.1698
Fe@$_{n\text{-}h}$S	382.27	338.27	44.00	0.3075	0.1564
Fe@$_{n\text{-}h}$S-HT	334.10	290.15	43.95	0.2930	0.1540

Notes: [a] determined by the BET method; [b] calculated by the t-plot method; [c] calculated using "S_{BET}—S_{micro}"; [d] results taken from the N_2 adsorbed at p/p_0 = 0.95.

2.2. HAADF-STEM and XRD Experiments

Figure 2 displays the HAADF-STEM micrographs obtained for the fresh catalysts. The images in Figure 2 correspond to the Fe/S, Fe@$_{n\text{-}h}$S, and Fe@$_{n\text{-}h}$S-HT samples, respectively. The TEM graphs of the Fe/S catalyst showed that a large block of Fe_2O_3 accumulated outside the zeolite particle. The corresponding EDS mapping images also showed that the Fe element was not uniformly distributed in the zeolite. In contrast, it is not difficult to find that the Fe element in the Fe@$_{n\text{-}h}$S and Fe@$_{n\text{-}h}$S-HT samples was highly dispersed in the zeolite. For the Fe@$_{n\text{-}h}$S, there were no metal nanoparticles to be found in the high-resolution TEM image F1, but there were clear lattice fringes of ZSM-5, indicating that the Fe species did not encapsulate into the micropores or channel of the S-1 zeolite in the form of FeO_x particles but was likely to occupy the skeleton site of the zeolite. Furthermore, the distribution of Si, O, and Fe in the EDS mapping images was highly overlapped, confirming that Fe entered the skeleton site of the S-1 zeolite frameworks. TEM image F2 showed visible nanoparticles with a size of 3.4 nm that were uniformly distributed in the hexagonal zeolite particle. At the same time, in the high-resolution mode of the dark field, no lattice fringes of the zeolite were found. It could be determined that the skeleton Fe sites of Fe@$_{n\text{-}h}$S in the sample transformed into Fe_2O_3 nanoclusters after the water steam treatment, which contributed to enhancing the FT reaction activity.

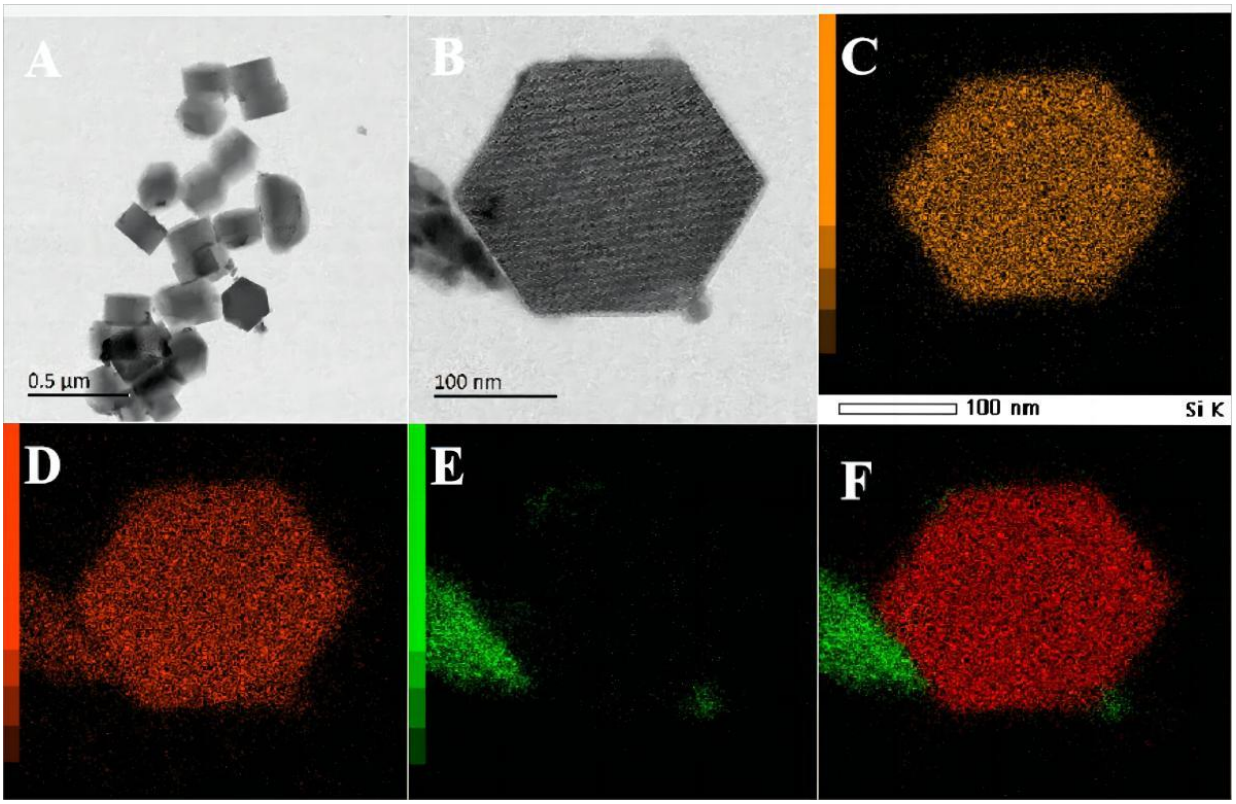

Figure 2. *Cont.*

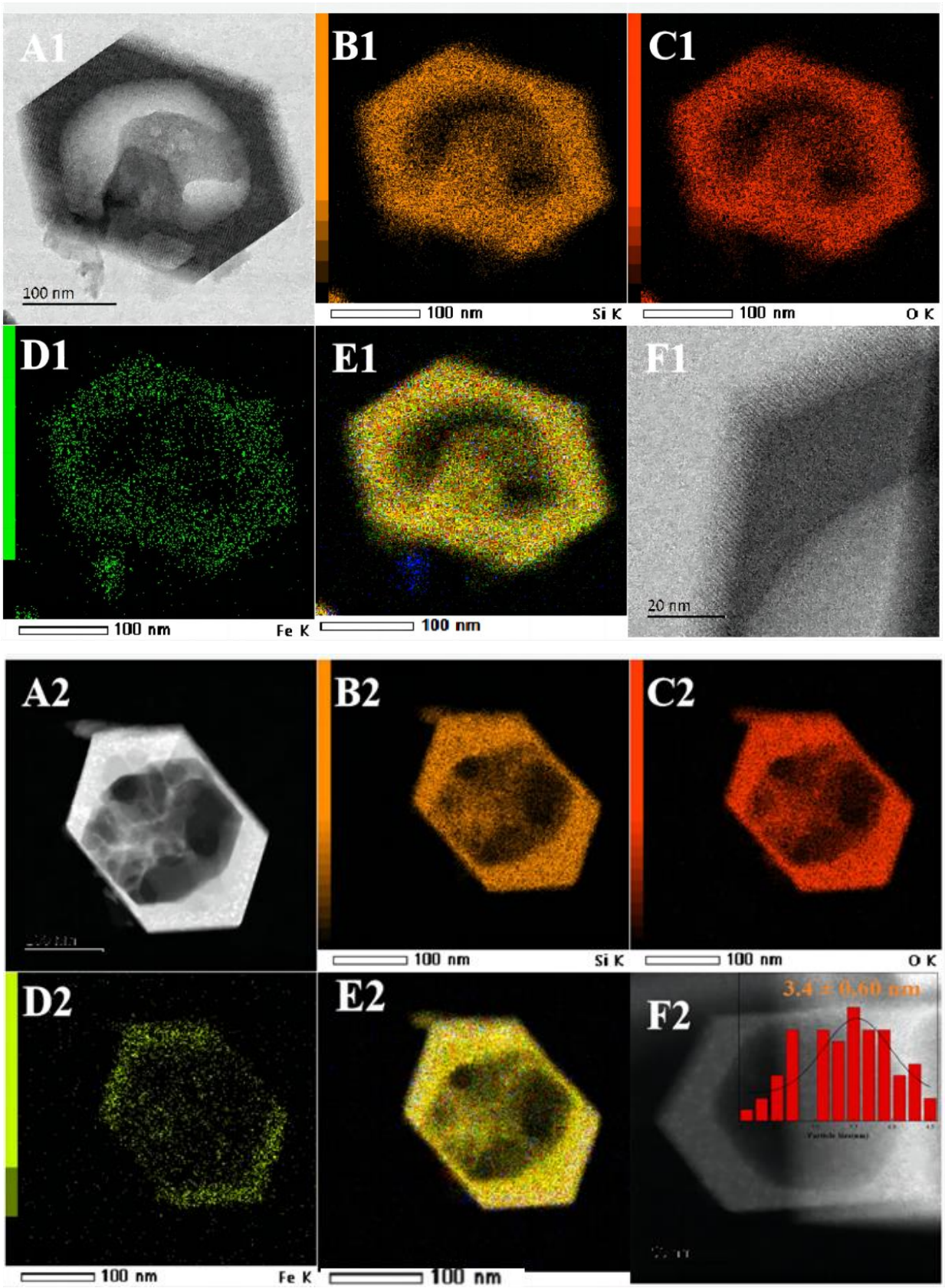

Figure 2. AC-HAADF-STEM and corresponding EDS mapping images of (**A**–**F**) Fe/S, (**A1**–**F1**) Fe@$_{n\text{-}h}$S, and (**A2**–**F2**) Fe@$_{n\text{-}h}$S-HT (the insert in **F2** shows particle size distribution, and the white dots in the yellow-dotted circle are nanoparticles observed under TEM).

The XRD data obtained for all the samples are shown in Figure 3. All the samples exhibited characteristic diffraction peaks at 2θ = 7.96°, 8.82°, 23.08°, 23.97°, and 24.43°, corresponding, respectively, to the (011), (200), (501), (033), and (133) facets of the Silicalite-1 zeolite (PDF#44-969) [5]. To characterize the change in relative crystallinity, the 2θ = 22.5°~25° of the standard ZSM-5 sample was selected as a reference, and its crystallinity was assumed to be100%. The relative crystallinity of the other samples was calculated as follows and presented in Figure 3A: The parent S-1 presented the highest relative crystallinity among all the samples. However, the other catalyst samples presented a lower crystallinity, indicating that some zeolite frameworks were destroyed during the process of loading metals. In addition, there was little change in relative crystallinity among the different catalysts. Compared to Fe@$_{n\text{-}h}$S, the crystallinity of Fe@$_{n\text{-}h}$S-HT only decreased by 2.86%, demonstrating that the shedding of the skeleton Fe had little damage to the integrity of the zeolite structure during the high-temperature steam treatment process. A closer observation of the XRD patterns (Figure 3B) shows that all catalysts possess peaks at around 2θ = 35.61°, which is consistent with the (110) facet of the α-Fe_2O_3 phase (PDF#85-0599), and the intensity of the diffraction peak increases with the sequence Fe/S > Fe@$_{n\text{-}h}$S-HT > Fe@$_{n\text{-}h}$S. In addition, except for the Fe/S catalyst, there are no obvious (104) and (024) peaks, corresponding to 2θ = 33.14° and 49.43° in both Fe@$_{n\text{-}h}$S and Fe@$_{n\text{-}h}$S-HT, respectively. These results fully demonstrate that the dispersion of Fe species on Fe@$_{n\text{-}h}$S and Fe@$_{n\text{-}h}$S-HT is significantly better than that of Fe/S. At the same time, there is more α-Fe_2O_3 phase in the Fe@$_{n\text{-}h}$S-HT catalyst than in Fe@$_{n\text{-}h}$S, indicating that the skeleton Fe species of the zeolite transformed into α-Fe_2O_3 nanoparticles via high water steam treatment on the Fe@$_{n\text{-}h}$S sample, which is consistent with the results of N_2-BET and HAADF-STEM.

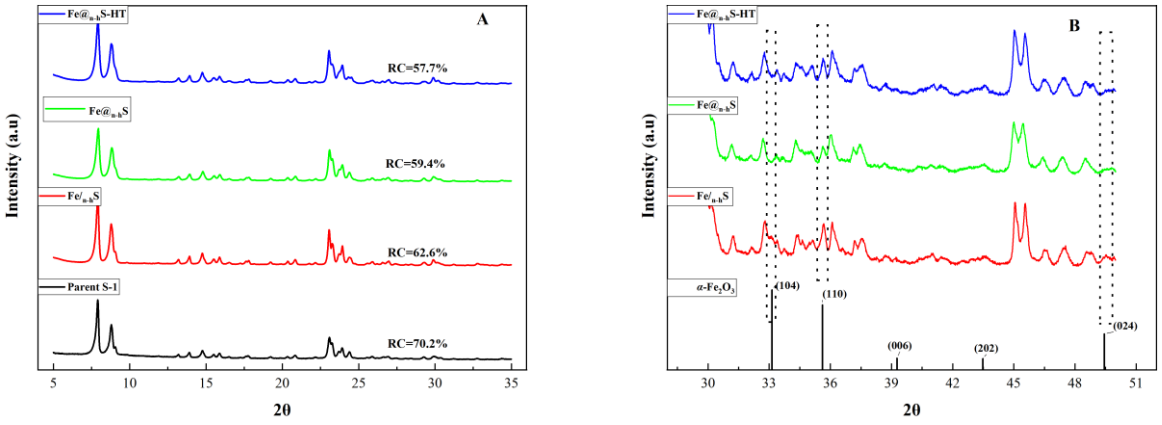

Figure 3. XRD patterns of parent S-1 zeolite and series catalysts: (**A**) the relative crystallinity of samples; (**B**) the Phase information of the samples.

The unit cell parameters and volume of different samples are shown in Table 2. Compared with the sample parent S-1, the cell parameters and the unit cell volume of the sample Fe/S changed little. This indicated no skeleton Fe in the sample Fe/S, prepared via impregnation. There was a significant increase in the unit cell volume of the sample and the parameters a, b, and c when going from Fe/S to Fe@$_{n\text{-}h}$S, indicating Fe entered the skeleton of the zeolite during the dissolution–recrystallization process. In addition, the significant decrease in the parameters and unit cell volume from Fe@$_{n\text{-}h}$S to Fe@$_{n\text{-}h}$S-HT showed the shedding of the skeleton Fe. On further observation of the unit cell parameters of the Fe@n-hS and Fe@n-hS-HT samples, it was not difficult to find the changes mainly concentrated on the parameters b and c, which may indicate that the steam treatment has more effects on the shedding of the skeleton Fe distributed along the b and c axes.

Table 2. Unit cell parameters and volume of different samples.

Samples	a (Å)	b (Å)	c (Å)	Unit Cell Volume (Å^3)
Parent S-1	20.1174	19.9213	13.4036	5371.66
Fe/S	20.1181	19.9228	13.4081	5374.09
Fe@$_{n\text{-}h}$S	20.1349	19.9588	13.4460	5403.54
Fe@$_{n\text{-}h}$S-HT	20.1366	19.9263	13.4173	5383.69

Notes: Calculated using Topas software.

The chemical compositions of the samples analyzed by XRF and XPS are also listed in Table 3. XPS is a surface technique with an analysis depth of <10 nm, and XRF can analyze the bulk composition; therefore, XPS/XRF can be used to characterize the distribution of Fe on the sample surface and inside the cavity of the zeolite [19–22]. By comparing the results of XPS/XRF, the Fe@$_{n\text{-}h}$S and Fe@$_{n\text{-}h}$S-HT samples had smaller ratios than the Fe/S sample, which further confirms that the Fe species were successfully encapsulated into the S-1 zeolite. These results are consistent with the HAADF-STEM images.

Table 3. Metal loading and Dispersion.

Samples	Metal Content [a]/%	Fe/Si [b]		XPS/XRF	d_{Fe} (nm)
	Fe	XPS [c]	XRF		
Fe/S	4.72	0.104	0.081	1.28	40.8
Fe@$_{n\text{-}h}$S	4.69	0.038	0.054	0.70	-
Fe@$_{n\text{-}h}$S-HT	4.43	0.042	0.056	0.75	3.4

Notes: [a] calculated by XRF; [b] molar ratio of Fe to Si; [c] determined using Fe/Si = $(I_{Fe}/f_{Fe})/(I_{Si}/f_{Si})$, where I is the peak area of XPS and f is the atom sensitivity of the factor. In this work, f_{Fe} = 2.957 and f_{Si} = 0.328. d calculated based on the α-Fe_2O_3 (104) facet using Scherrer's Equation.

2.3. H_2-TPR Experiments

The reducibility of the different catalysts is exhibited in Figure 4. Compared to Fe/S, the peaks of Fe@$_{n\text{-}h}$S and Fe@$_{n}$-hS-HT shifted to a higher temperature, which might be due to the strong metal–Si interaction derived from the encapsulated structure catalysts that suppressed the reduction of metal oxide [13,15]. Additionally, due to the diversity of interactions between Fe and the zeolite, the reducibility peaks of H_2-TPR were relatively complex. The reducibility peaks of the iron species in Fe–zeolite could be divided into the following categories [23]: i. peaks in the 320–377 °C range were F(III) (isolated Fe(III), Fe_xO_y, α-Fe_2O_3 nanoparticles) reduced to Fe(II)); ii. peaks in the 350–500 °C range were extra-framework F(III) to Fe(II); iii. peaks in the 500–640 °C range were framework Fe(III) to Fe(II); iii. peaks in the 500–640 °C range were framework F(III) to Fe(II); iv. peaks in the 427–627 °C range were FeO to Fe^0; v. peaks >800 °C were attributed to Fe(II) to Fe^0 with collapse of the zeolite framework. Therefore, it can be inferred that the peak δ_1 of the Fe@$_{n\text{-}h}$S and Fe@$_{n\text{-}h}$S-HT samples can be attributed to the framework Fe species, and peaks α and β in all samples can be attributed to the reduction of Fe_2O_3 to FeO. After fitting the reduction peaks of the different Fe species, the quantity percentage of the peak area for each corresponding peak was determined and is shown in Table 4. The fitting results indicated that the Fe@$_{n\text{-}h}$S and Fe@$_{n\text{-}h}$S-HT samples possessed skeleton Fe species compared to Fe/S. The decrease in the value of the area responding to the δ_1 peak of Fe@$_{n\text{-}h}$S-HT compared with Fe@$_{n\text{-}h}$S also demonstrated the transformation of skeleton Fe species into α-Fe_2O_3 nanoparticles after high water steam treatment, which was consistent with the results of HAADF-STEM and XRD.

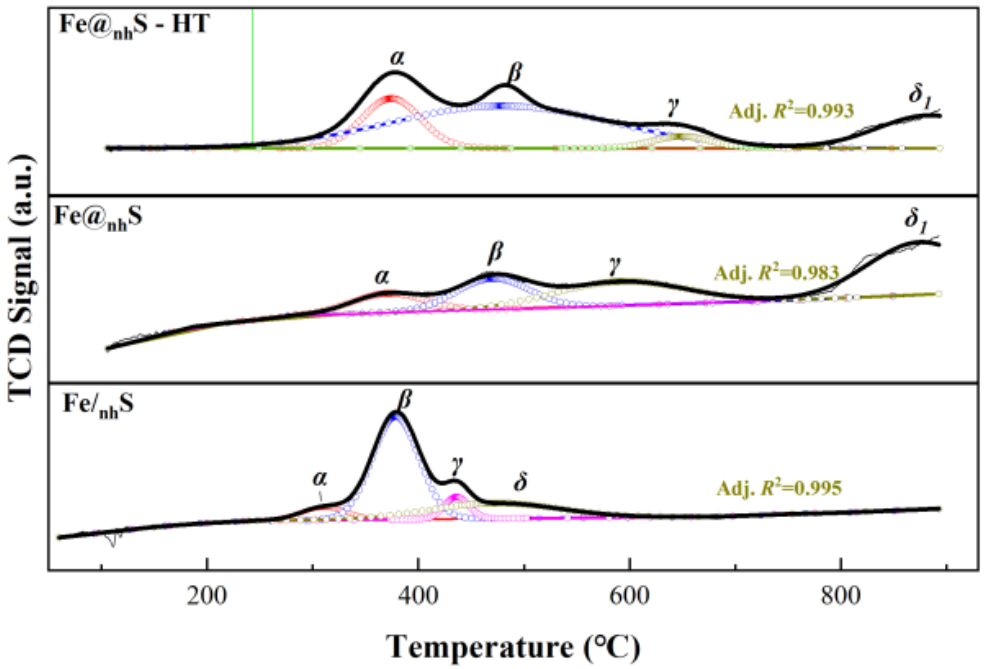

Figure 4. H_2-TPR profiles of different catalysts.

Table 4. The results of fitting peaks of different catalysts.

Samples	Peak α % (°C)	Peak β % (°C)	Peak γ % (°C)	Peak δ (or δ_1) % (°C)
Fe/S	7.43% (310.8)	60.51% (378.5)	6.81% (436.1)	25.25% (472.6)
Fe@$_{n\text{-}h}$S	13.43% (339.5)	21.66% (444.0)	30.42% (572.1)	34.49% (871.3)
Fe@$_{n\text{-}h}$S-HT	18.41% (342.8)	64.40% (453.5)	4.47% (633.0)	12.72% (881.6)

Notes: The numbers in parentheses represent temperature.

2.4. Catalytic Performance

Figure 5 shows the FT synthesis catalytic performance for catalysts with different configurations at 6750 mL/(g.h) and H_2/CO = 2/1. Figure 5A,B display the catalytic activity and stability of all the catalysts in the time stream from 0 h to 75 h. The reaction activity of all the samples increased according to the sequence Fe/S > Fe@$_{n\text{-}h}$S-HT > Fe@$_{n\text{-}h}$S, resulting from the quantity of α-Fe_2O_3, which is the active phase of the FT reaction. In addition, it was not difficult to find that the Fe@$_{n\text{-}h}$S-HT catalyst possessed better selectivity (21.38%) and FTY of C_2-$C_4^=$ (13.26 umol/(g_{Fe}. S)) than the other two catalysts according to Figure 5C,D, derived from the selective catalytic uniqueness of the S-1 zeolite and the confinement effect of Fe@$_{n\text{-}h}$S-HT with an encapsulated structure. These catalytic performances were utterly consistent with the characterization results of H_2-TPR, HAADF-STEM, and XRD. In general, the catalytic stability of all the catalysts was good during the long reaction time of 75 h.

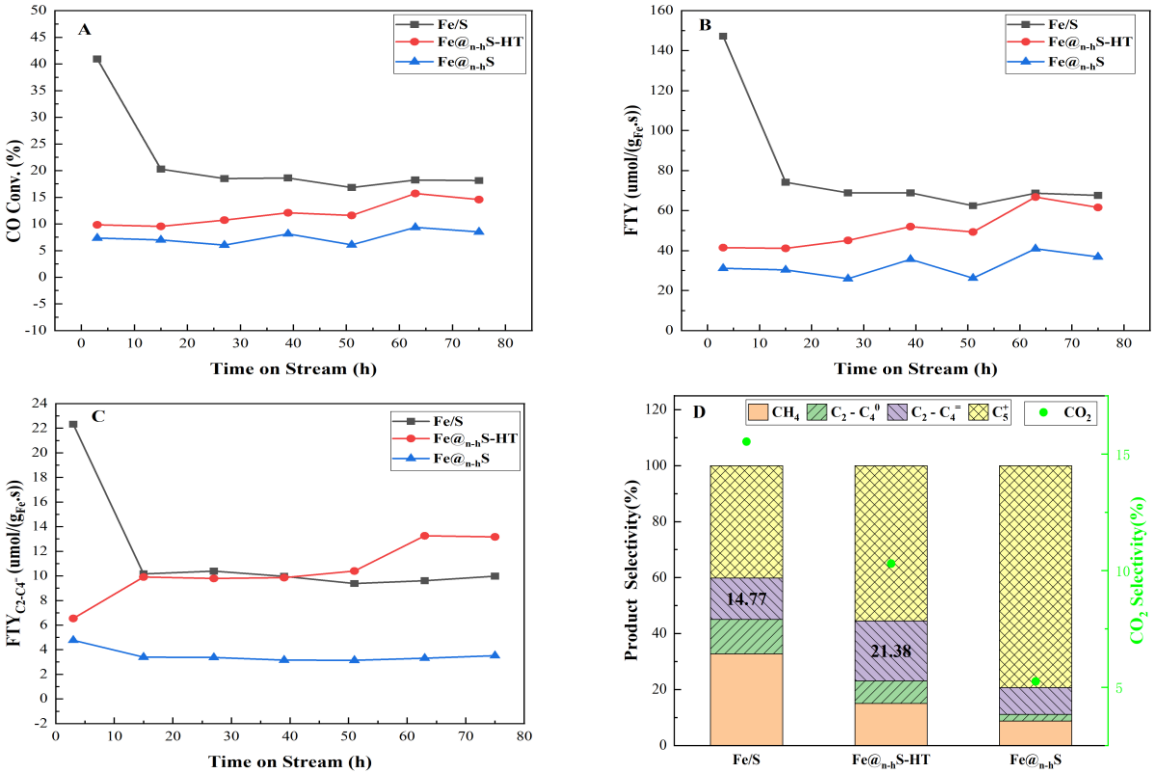

Figure 5. Catalytic performance for the samples: (**A**) the conversion of CO; (**B**) the molar yield of total hydrocarbons per gram of catalyst (FTY); (**C**) the molar yield of C_2-$C_4^=$ per gram of catalyst; (**D**) product distribution. Reaction conditions: 340 °C, 6750 mL/(g.h), 10 bar, H_2/CO/He = 6/3/1.

3. Experimental Section

3.1. Materials

Tetrapropylammonium hydroxide solution (TPAOH, 25%), ethyl orthosilicate (TEOS, AR), and $Fe(NO_3)_3 \cdot 9H_2O$ were purchased from Shanghai Aladdin Bio-Chem Technology Co., Ltd., Shanghai, China.

3.2. Catalysts Preparation

3.2.1. Synthesis of Parent S-1 Zeolite

Silicalte-1 zeolite was synthesized by the clear solution method [13] with a molar ratio of $1SiO_2$: 0.4TPAOH: $37H_2O$. Typically, 10.00 g TEOS, 15.30 g TPAOH, and 18.21 g deionized water were mixed in a 100 mL beaker under stirring at room temperature for 6 h. Then, the above mixture was transferred to a 100 mL Teflon-lined steel autoclave, followed by crystallization at 180 °C for 48 h. The as-synthesized silicalite-1 zeolite was collected via centrifugation and dried overnight at 110 °C. Finally, the zeolite sample was calcined in a muffle furnace at 550 °C for 4 h to remove the organic template.

3.2.2. Synthesis of Fe/S Catalyst

The Fe/S catalyst was synthesized by an impregnation method. Briefly, the parent S-1 zeolite was impregnated with $Fe(NO_3)_3$ solution. After impregnation, the sample was dried at 110 °C for 12 h and then calcined at 450 °C for 4 h. The catalyst obtained was named Fe/S. The theoretical Fe loading was 4%.

3.2.3. Preparation of Fe@ $_{n\text{-}h}$S and Fe@ $_{n\text{-}h}$S-HT Catalysts

The Fe@$_{n\text{-}h}$S catalyst was synthesized by the dissolution–recrystallization (DR) method [13,14]. In brief, the as-prepared Fe/S catalyst was treated with TPAOH solution at 170 °C for 24 h, and the molar ratio of SiO_2:TPAOH:H_2O was 1:0.26:24. After being

cooled to room temperature, the products were recovered by centrifugation and washed to a pH of 7.0 with deionized water. Then the sample was dried overnight at 110 °C and calcined at 450 °C for 6 h. The final sample obtained was denoted Fe@$_{n\text{-}h}$S. In order to transform the Fe species substituted in zeolite frameworks into FeO_x species, the as-prepared Fe@$_{n\text{-}h}$S sample was further treated with 400 °C water steam for 12 h, and the final sample was named Fe@$_{n\text{-}h}$S-HT. The theoretical Fe loadings of the above two catalysts were 4%.

3.3. Catalyst Characterization

The textural properties of different configurational catalysts were measured through the N_2 adsorption and desorption experiment, which was performed on the Micromeritics ASAP 2420 instrument. Before the experiment, all samples were degassed under vacuum at 350 °C for 12 h. The Brunauer–Emmett–Teller (BET) method was applied for calculating the total surface area. The micro- and mesopores were calculated via the t-plot method. In addition, the pore volume and average pore size of catalysts were calculated using the Barrett–Joyner–Halenda (BJH) model. Powder X-ray diffraction (XRD) patterns were collected on a D/MAX-III type powder diffractometer (PANalytical Corporation, Netherlands) using Cu K*a* radiation (λ = 0.154 nm) at a scanning rate of 2°/min from 20° to 70°.

The elemental chemical compositions of the configurational catalysts were measured using an X-ray fluorescence (XRF) spectrometer (Rigaku Primus II). The X-ray photoelectron spectroscopy (XPS) characterizations were carried out on a Thermo ESCALAB 250 XI spectrometer equipped with an Al K*a* X-ray radiation source. Each element was calibrated via a C 1 s peak at 284.8 eV.

The morphology and energy-dispersive spectroscopy (EDS) mapping of all the catalysts were analyzed using a JEOL JEL-ARM 200 F special aberration-corrected transmission electron microscope under the condition of high-angle annular dark field (HAADF-STEM).

The reducibility of samples was characterized through H_2 Temperature Programmed Reduction (H_2-TPR) method experiments conducted on a Micromeritics AutoChem II 2920 analyzer fitted with a thermal conductivity detector (TCD). A total of 200 mg of the catalysts (40~60 mesh) was used in every H_2-TPR experiment. The sample was pretreated at 120 °C for 30 min in argon (Ar) flow to remove the impurities. After that, the sample was heated to 900 °C at a rate of 5 °C/min in a 10% H_2-Ar flow (50 mL/min), and the reduced data were recorded with TCD.

3.4. Catalytic Evaluation

The FTS catalytic performance of different configurational catalysts was carried out on a high-throughput reaction system (Avantium B.V) for the conversion of light hydrocarbons, on which 16 microreactors (length (300 mm) × inside diameter (2 mm)) can be performed in parallel. Typically, 40 mg catalysts with grain sizes of 60–80 mesh were mixed with 360 mg SiC (60~80 mesh). The above mixture was then added to the isothermal region of the reactors. All the samples were reduced in a 50% H_2/N_2 stream flowing at a rate of 100 mL·min^{-1} at 400 °C for 3 h under atmospheric pressure. After cooling down to room temperature, the reactors were pressurized with syngas (H_2/CO/He = 60/30/10) to 10 bar and heated to the specified temperature at a rate of 2 °C·min^{-1}. The tail gas was analyzed using an Agilent 7890B gas chromatograph equipped with a FID detector and a TCD detector. Helium in the feed gas was assumed to be an internal standard during the reaction. The conversion and selectivity were calculated using the following equation:

$$X_{CO} = \frac{V_{CO,in} - V_{CO,out}}{V_{CO,in}} \times 100\% \quad (1)$$

$$S_{CO_2} = \frac{V_{CO_2,out}}{V_{CO,in} - V_{CO,out}} \times 100\% \quad (2)$$

$$S_{C_i} = \frac{i \times V_{C_i,out}}{V_{CO,in} - V_{CO,out} - V_{CO_2,in}} \times 100\% \quad (3)$$

$$S_{C_5^+} = (1 - \sum_{i=1}^{4} C_i) \times 100\% \quad (4)$$

The words "*in*" and "*out*" in the above equation represent gas that flows into or out of the reactor. The FTY of the catalyst, which is defined as the yield of CO converted to hydrocarbons per gram of Fe per second, was calculated using the equation below:

$$FTY = \frac{V_{CO,in} \times X_{CO} \times (1 - S_{CO_2})}{V_m \times m \times W_{Fe}} \quad (5)$$

"V_m" in the above equation represents the molar volume of ideal gas under standard conditions, of which the value is 22.4 L/mol; "m" is the mass of the catalyst loaded in the reactor; and "W_{Fe}" is the mass fraction of Fe elements in the catalyst, which is derived from the XRF results.

The FTY of C_2–$C_4^=$ in the products was calculated using the equation below:

$$FTY_{C_2-C_4^=} = FTY \times S_{C_2-C_4^=} \quad (6)$$

where "$S_{C_2-C_4^=}$" is the selectivity of light olefins.

4. Conclusions

Hollow hierarchical Fe@$_{n\text{-}h}$S and Fe@$_{n\text{-}h}$S-HT catalysts were successfully synthesized through the dissolution–recrystallization (D-R) method for the Fischer–Tropsch synthesis reaction. The encapsulated catalysts Fe@$_{n\text{-}h}$S and Fe@$_{n\text{-}h}$S-HT, which had hierarchical porous structures, possessed better dispersion of Fe species compared to the Fe/S catalyst prepared via the conventional impregnation method. Moreover, compared to the Fe/S catalyst, the Fe@$_{n\text{-}h}$S-HT catalyst showed higher FTY and selectivity of C_2-$C_4^=$ at the conditions investigated in this work due to the shape-selective catalysis of the metal@zeolite catalyst and its confined catalytic effect on ultra-fine nano-Fe_2O_3 particles. Furthermore, through a mild water steam aging treatment of the catalyst Fe@$_{n\text{-}h}$S, the skeleton Fe species could indeed be converted into nano-Fe_2O_3 particles encapsulated in the pores of the zeolite, which provided an effective way to solve the problem of Fe species being easy to substitute in the zeolite framework with the assistance of organic templates and to prepare zeolite-encapsulated Fe nanocatalysts. In summary, the evaluation of the above catalysts and all the characterization results confirmed the confined catalysis of the metal@zeolite catalyst and its superiority in improving the yield of light olefins in the FT reaction. This work provides some optimistic prospects for designing high-exhibition catalysts for the FT reaction and even other heterogeneous catalytic reactions.

Author Contributions: Conceptualization, E.X., Y.W. (Yu Wu) and Z.D.; Methodology, E.X., Y.W. (Yu Wu) and Z.D.; Investigation, R.H.; Resources, Y.W. (Yifan Wang), T.W., L.X., E.X., Y.W. (Yu Wu) and Z.D.; Data curation, R.H., Y.W. (Yifan Wang) and T.W.; Writing—original draft, R.H.; Writing—review & editing, R.H.; Project administration, E.X., Y.W. (Yu Wu) and Z.D.; Funding acquisition, Z.D., E.X., Y.W. (Yu Wu) and Y.Z. All authors have read and agreed to the published version of the manuscript.

Funding: This work was supported by the China Petrochemical Group Headquarters Project "Research on synergistic catalysis of oil-soluble additives to produce low-carbon olefins (ST19010-4-022)"Fund from the China Petrochemical Group Headquarters.

Data Availability Statement: Not applicable.

Conflicts of Interest: The authors declare that they have no known competing financial interest or personal relationships that could have appeared to influence the work reported in this paper.

References

1. Zhang, Q.; Gao, S.; Yu, J. Metal Sites in Zeolites: Synthesis, Characterization, and Catalysis. *Chem. Rev.* **2022**, *123*, 6039–6106. [CrossRef] [PubMed]
2. Gao, C.; Lyu, F.; Yin, Y. Encapsulated Metal Nanoparticles for Catalysis. *Chem. Rev.* **2021**, *121*, 834–881. [CrossRef] [PubMed]
3. Zhang, J.; Wang, L.; Zhang, B.; Zhao, H.; Kolb, U.; Zhu, Y.; Liu, L.; Han, Y.; Wang, G.; Xiao, F.S.; et al. Sinter-resistant metal nanoparticle catalysts achieved by immobilization within zeolite crystals via seed-directed growth. *Nat. Catal.* **2018**, *1*, 540–546. [CrossRef]
4. Babucci, M.; Guntida, A.; Gates, B.C. Atomically Dispersed Metals on Well-Defined Supports including Zeolites and Metal–Organic Frameworks: Structure, Bonding, Reactivity, and Catalysis. *Chem. Rev.* **2020**, *120*, 11956–11985. [CrossRef]
5. Niu, X.; Li, X.; Yuan, G.; Feng, F.; Wang, M.; Zhang, X.; Wang, Q. Hollow Hierarchical Silicalite-1 Zeolite Encapsulated PtNi Bimetals for Selective Hydroconversion of Methyl Stearate into Aviation Fuel Range Alkanes. *Ind. Eng. Chem. Res.* **2020**, *59*, 8601–8611. [CrossRef]
6. Liu, Y.; Chen, Y.; Gao, Z.; Zhang, X.; Zhang, L.; Wang, M.; Chen, B.; Diao, Y.; Li, Y.; Shi, C.; et al. Embedding high loading and uniform Ni nanoparticles into silicalite-1 zeolite for dry reforming of methane. *Appl. Catal. B Environ.* **2022**, *307*, 121202. [CrossRef]
7. Zhang, F.; Zhou, W.; Xiong, X.; Wang, Y.; Cheng, K.; Kang, J.; Zhang, Q.; Wang, Y. Selective Hydrogenation of CO_2 to Ethanol over Sodium-Modified Rhodium Nanoparticles Embedded in Zeolite Silicalite-1. *J. Phys. Chem. C* **2021**, *125*, 24429–24439. [CrossRef]
8. Yang, Z.; Li, H.; Zhou, H.; Wang, L.; Wang, L.; Zhu, Q.; Xiao, J.; Meng, X.; Xiao, F.S. Coking-Resistant Iron Catalyst in Ethane Dehydrogenation Achieved through Siliceous Zeolite Modulation. *J. Am. Chem. Soc.* **2020**, *142*, 16429–16436. [CrossRef]
9. Gao, Y.; Wei, Y.; Sun, W.; Zhao, G.; Liu, Y.; Lu, Y. Insight into deactivation of the carbon-/sintering-resistant Ni@Silicalite-1 for catalytic partial oxidation of methane to syngas. *Fuel* **2022**, *320*, 123892. [CrossRef]
10. Gao, J.; Wu, Y.; Jia, C.; Zhong, Z.; Gao, F.; Yang, Y.; Liu, B. Controllable synthesis of alpha-MoC1-x and beta-Mo2C nanowires for highly selective CO_2 reduction to CO. *Catal. Commun.* **2016**, *84*, 147–150. [CrossRef]
11. Song, W.; Zhang, B.; Chen, L.; Shi, J.; Cheng, X.; Wu, L.; Yang, W.; Zhou, J.; Zhang, Y.; Tang, Y.; et al. An Fe–Mn–Cu/SiO_2 @silicalite-1 catalyst for CO hydrogenation: The role of the zeolite shell on light-olefin production. *Catal. Sci. Technol.* **2016**, *6*, 3559–3567. [CrossRef]
12. Zhu, C.; Zhang, M.; Huang, C.; Zhong, L.; Fang, K. Carbon-encapsulated highly dispersed FeMn nanoparticles for Fischer–Tropsch synthesis to light olefins. *New J. Chem.* **2018**, *42*, 2413–2421. [CrossRef]
13. Dai, C.; Zhang, A.; Luo, L.; Zhang, X.; Liu, M.; Wang, J.; Guo, X.; Song, C. Hollow zeolite-encapsulated Fe-Cu bimetallic catalysts for phenol degradation. *Catal. Today* **2017**, *297*, 335–343. [CrossRef]
14. Li, S.; Tuel, A.; Laprune, D.; Meunier, F.; Farrusseng, D. Transition-Metal Nanoparticles in Hollow Zeolite Single Crystals as Bifunctional and Size-Selective Hydrogenation Catalysts. *Chem. Mater.* **2015**, *27*, 276–282. [CrossRef]
15. Zhu, C.; Zhang, M.; Huang, C.; Han, Y.; Fang, K. Controlled Nanostructure of Zeolite Crystal Encapsulating FeMnK Catalysts Targeting Light Olefins from Syngas. *ACS Appl. Mater. Interfaces* **2020**, *12*, 57950–57962. [CrossRef]
16. Wang, Y.; Lin, M.; Tuel, A. Hollow TS-1 crystals formed via a dissolution–recrystallization process. *Microp. Mesoporous Mater.* **2007**, *102*, 80–85. [CrossRef]
17. Dai, C.; Zhang, A.; Liu, M.; Guo, X.; Song, C. Hollow ZSM-5 with Silicon-Rich Surface, Double Shells, and Functionalized Interior with Metallic Nanoparticles and Carbon Nanotubes. *Adv. Funct. Mater.* **2015**, *25*, 7479–7487. [CrossRef]
18. Wei, F.F.; Liu, J.; Zhang, Q.Y.; Zhang, Y.T.; Zhang, X.; Cao, C.Y.; Song, W.G. Sharp size-selective catalysis in a liquid solution over Pd nanoparticles encapsulated in hollow silicalite-1 zeolite crystals. *RSC Adv.* **2016**, *6*, 89499–89502. [CrossRef]
19. Kwok, K.M.; Ong, S.W.D.; Chen, L.; Zeng, H.C. Transformation of Stöber Silica Spheres to Hollow Hierarchical Single-Crystal ZSM-5 Zeolites with Encapsulated Metal Nanocatalysts for Selective Catalysis. *ACS Appl. Mater. Interfaces* **2019**, *11*, 14774–14785. [CrossRef]
20. Cui, T.L.; Ke, W.Y.; Zhang, W.B.; Wang, H.H.; Li, X.H.; Chen, J.S. Encapsulating Palladium Nanoparticles Inside Mesoporous MFI Zeolite Nanocrystals for Shape-Selective Catalysis. *Angew. Chem. Int. Ed.* **2016**, *55*, 9178–9182. [CrossRef]
21. Liu, G.; Tian, Y.; Zhang, B.; Wang, L.; Zhang, X. Catalytic combustion of VOC on sandwich-structured Pt@ZSM-5 nanosheets prepared by controllable intercalation. *J. Hazard. Mater.* **2019**, *367*, 568–576. [CrossRef] [PubMed]
22. Alov, N.V. Determination of the States of Oxidation of Metals in Thin Oxide Films by X-ray Photoelectron Spectroscopy. *J. Anal. Chem.* **2005**, *60*, 431–435. [CrossRef]
23. Zhang, J.; Tang, X.; Yi, H.; Yu, Q.; Zhang, Y.; Wei, J.; Yuan, Y. Synthesis, characterization and application of Fe-zeolite: A review. *Appl. Catal. A Gen.* **2022**, *630*, 118467. [CrossRef]